1 Electronic Supplementary Information

2 Atmospheric Aging Modifies the Redox Potential and Toxicity of Humic-like Substances
3 from Biomass Burning

4 Chunlin Li [a, e], Diego Calderon-Arrieta [b], Michal Pardo [a], Dongmei Cai [c], Alexander Laskin [b, d], Jianmin Chen [c], Yinon

5 Rudich [a,*]

6 [a] Department of Earth and Planetary Sciences, Weizmann Institute of Science, Israel, 7600001.

7 [b] Department of Chemistry, Purdue University, West Lafayette, USA 47907.
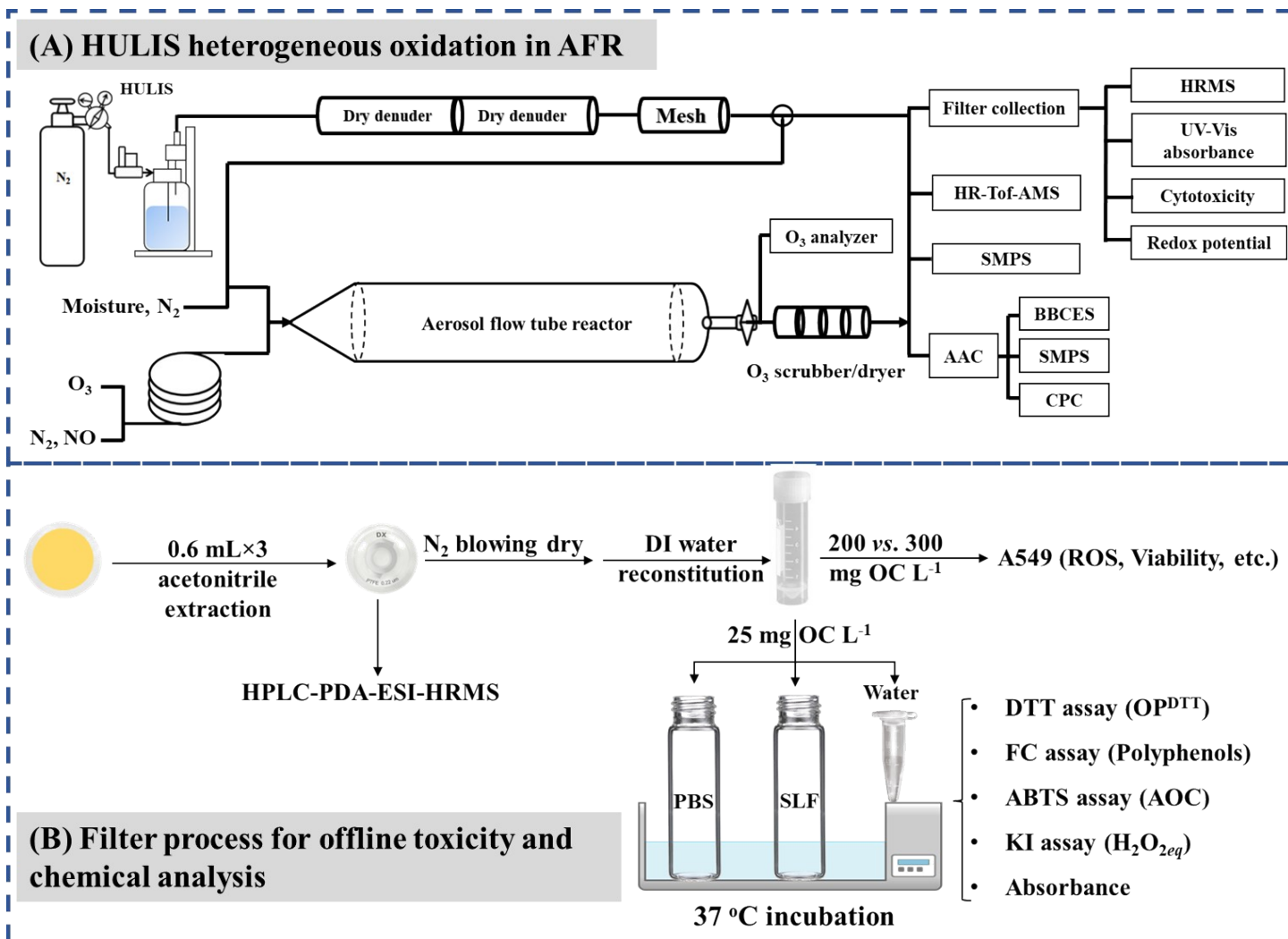
8 [c] Department of Environmental Science & Engineering, Fudan University, Shanghai, China, 236400.

9 [d] Department of Earth, Atmosphere and Planetary Sciences, Purdue University, West Lafayette, USA 47907.

10 [e] College of Environmental Science and Engineering, Tongji University, Shanghai 200072, China

11 Corresponding author: Yinon Rudich (*yinon.rudich@weizmann.ac.il*)

12 Assisting details of chemical box modeling of atmospheric aging, acellular assays, elemental quantification,

13 molecular analysis, and lifetime assessment of HULIS together with standard redox-active compounds test in

14 lung fluid mimics are provided in SI, including **8 texts, 16 figures and 2 tables**.

(A) HULIS heterogeneous oxidation in AFR

(B) Filter process for offline toxicity and chemical analysis

Fig. S1. (A) A schematic representation of the experimental setup and methods for HULIS aerosol generation, heterogeneous aging, online characterization, and filter sampling. (B) Scheme of treatment and offline analysis of filter-loaded for chemical composition, redox potential, and cytotoxicity measurements.

Text S1. O_3 uptake coefficients and chemical-box model simulation of $NO_3\bullet$ aging

Three atmospheric nighttime aging scenarios, including *I.* dry ozonolysis (clean environment); *II.* O_3 oxidation under high RH; *III.* $NO_3\bullet$ dominated oxidation (simulating high NO_x (polluted) environment), were simulated using an aerosol flow tube reactor (AFR, Length: 180 cm, I.D: 10.5 cm) system and suspended HULIS aerosols. The total flow was fixed at 4 L min^{-1}. The Reynolds number (Re) was estimated to be around 510, indicating laminar flow ($Re < 2300$) in the AFR during the experiments.

For O_3 oxidation under high RH (*scenario I and II*), O_3 exposure and humidity (RH) level are important environmental factors. Their effects on the ozonolysis of HULIS were tested. Under dry conditions (RH<1.5%), the initial O_3 was set at 5, 15, and 25 ppmv. After that, RH was elevated stepwise to 30%, 45%, and 75% with a fixed initial O_3 of 25 ppmv. The changes of O_3 and particle concentrations were continuously monitored downstream of the AFR. Before the experiments, blank tests were conducted to characterize the reactants' loss to the inner wall of the AFR.

The ensemble first-order wall loss rates for O_3 ($\kappa_{w,O3}$, s^{-1}) and HULIS particles ($\kappa_{w,p}$, s^{-1}) were calculated using Equation S1 below:

$$\kappa_w = ln\left(\frac{C_0}{C}\right) / RT$$

Eq.S1

Where C_0 and C are the initial and endpoint pollutant concentration, respectively. RT (s) is the residence time of pollutants in the AFR. The estimated wall loss rates of O_3, particle surface area (S, μm^2 cm^{-3}), and volume (V, μm^3 cm^{-3}) concentrations are summarized in **Table S1**.

In the actual experiments where O_3 and HULIS aerosol are mixed in the AFR system, the sink of O_3 as described in Equation S2 includes wall loss ($\kappa_{w,O3}$) and particle surface uptake ($\kappa_{p,O3}$) [1,2]:

$$-\frac{dC_{O3}}{dt} = \kappa_{w,O3} \times C_{O3} + \kappa_{p,O3} \times C_{O3}$$

Eq.S2

Where $\kappa_{p,O3}$ can be expanded to Equation S3:

$$\kappa_{p,O3} = \frac{\gamma_{eff,O3} \times \omega_{O3} \times S_p}{4}$$

Eq.S3

In Eq.S3, $\gamma_{eff,O3}$ is the effective uptake coefficient of O_3. ω_{O3} is the mean thermal velocity of O_3 (361.12 m s^{-1} at 1 atm and 295K). S_p is total particle surface area concentration of $(3.0\text{-}3.6)\times10^4$ μm^2 cm^{-3}, which varied with time mainly due to particle wall loss, neglecting gas-particle transfer modification. Based on the known particle surface area concentration wall loss rates ($\kappa_{w,p-S}$, s^{-1}), Eq. S3 can be modified to Equation S4:

$$\kappa_{p,O3} = \frac{\gamma_{eff,O3} \times \omega_{O3} \times S \times e^{-\kappa_{w,p-S} \times t}}{4} = A \times e^{-\kappa_{w,p-S} \times t}$$

Eq.S4

S is the particles' initial surface area concentration. A is a simplified constant value that represents $\dfrac{\gamma_{eff,O3} \times \omega_{O3} \times S}{4}$. Eq S2 was further modified to give the final integrated function of Eq. S5:

$$ln\left(\frac{C_{O3,0}}{C_{O3,RT}}\right) = \kappa_{w,O3} \times RT + \frac{A}{\kappa_{w,p-S}} \times (1 - e^{-\kappa_{w,p-S} \times RT})$$

Eq.S5

Based on the O_3 concentration changes following mixing with the aerosol, the effective uptake coefficients of O_3 by HULIS aerosol were estimated and plotted in Figure S2. Clearly, the uptake coefficients are in range of 5.9×10^{-5} and
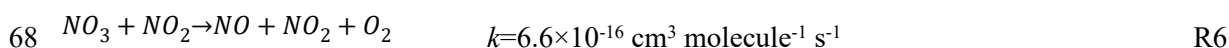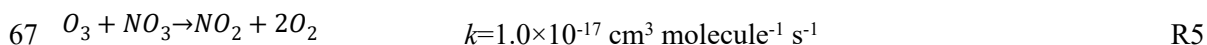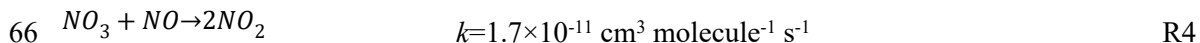
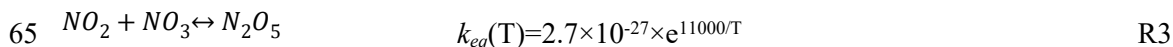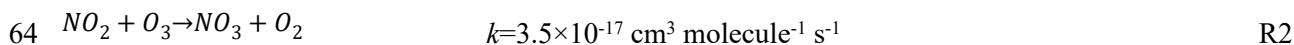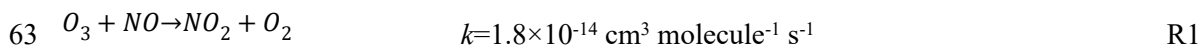50 1.8×10^{-4}, which are comparable with the reported values for soot and other organic aerosols and proxies.[3,4] The coefficients

51 vary exponentially in ascending trend with RH while in descending trend with initial O_3 concentration, agreeing with

52 previous studies.[5,6]
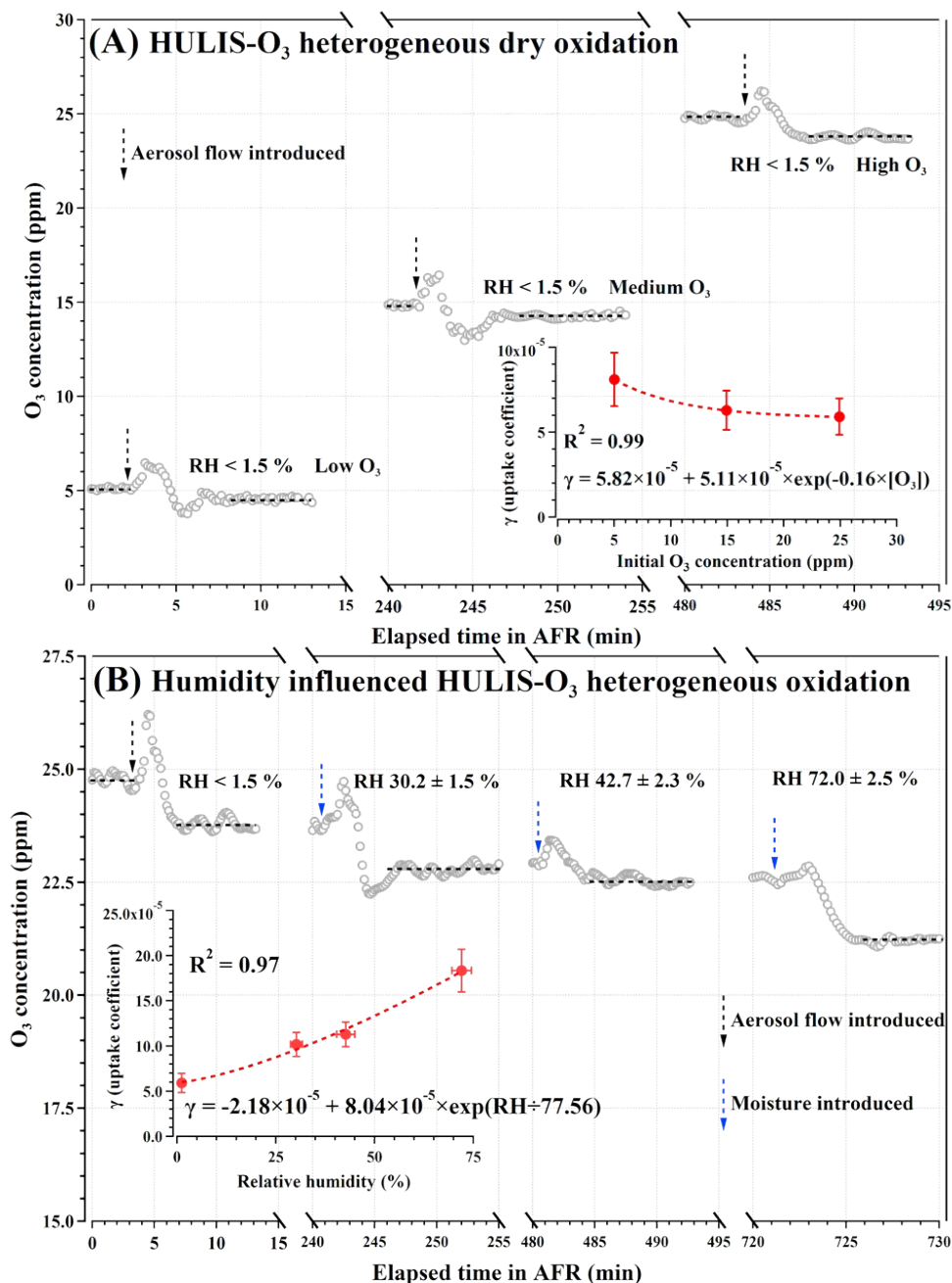
53 **Fig. S2**. Changes in O_3 concentration during the dry (A) and RH-dependent (B) ozonolysis of HULIS aerosols. Accordingly, the aerosol

54 effective uptake coefficients of O_3 were calculated in consideration of the pollutants' wall loss within the AFR. The insert figures plot

55 the HULIS particle uptake coefficients of O_3 as a function of the initial O_3 concentration and RH. These uptake coefficients were fitted

56 well using an exponential model.

57 **For NO$_x$ involved (NO$_3$•) heterogeneous aging (*scenario III*),** a similar method using a chemical box model simulation

58 of gaseous oxidants uptake by particles and gas-particle reactor inner wall has been built and applied in our previous

4

59 studies.[7,8] Here, the box model was modified by applying some measured parameters rather than theoretical values. Briefly,

60 flow from a calibrated cylinder NO (50 ppmv in high purity N_2, Gas Tech.) as NO_x source was first mixed with external O_3

61 flow through a long Teflon tube (I.D.:14 mm, Length: 2500 mm), where a series of oxidation reactions, especially reaction

62 R1-R3, occurred under dry condition (RH < 0.2%) to generate $NO_3\bullet$ and N_2O_5:

63 $O_3 + NO \rightarrow NO_2 + O_2$ $\qquad\qquad$ k=1.8×10^{-14} cm^3 molecule^{-1} s^{-1} $\qquad\qquad\qquad$ R1

64 $NO_2 + O_3 \rightarrow NO_3 + O_2$ $\qquad\qquad$ k=3.5×10^{-17} cm^3 molecule^{-1} s^{-1} $\qquad\qquad\qquad$ R2

65 $NO_2 + NO_3 \leftrightarrow N_2O_5$ $\qquad\qquad$ k_{eq}(T)=2.7×10^{-27}×e$^{11000/T}$ $\qquad\qquad\qquad$ R3

66 $NO_3 + NO \rightarrow 2NO_2$ $\qquad\qquad$ k=1.7×10^{-11} cm^3 molecule^{-1} s^{-1} $\qquad\qquad\qquad$ R4

67 $O_3 + NO_3 \rightarrow NO_2 + 2O_2$ $\qquad\qquad$ k=1.0×10^{-17} cm^3 molecule^{-1} s^{-1} $\qquad\qquad\qquad$ R5

68 $NO_3 + NO_2 \rightarrow NO + NO_2 + O_2$ $\qquad$ k=6.6×10^{-16} cm^3 molecule^{-1} s^{-1} $\qquad\qquad\qquad$ R6

69 Two "pollution" levels were investigated and termed as low and high NO_x (initially 1.0 $vs.$ 5.0 ppm NO into the AFR)

70 condition, resulting in corresponding mixing time of about 30 s and 15 s with O_3 in the Teflon tube. Afterward, the steady

71 flow of NO_y and O_3 mixtures was introduced into the AFR to mix with dehydrated HULIS aerosols. Similarly, apart from

72 gaseous reactions, the sink of these gaseous species ($\frac{d[G]}{dt}$) can also be attributed to the pseudo-first-order loss to the particles'

73 surface ($k_p[G]$) and to the AFR inner wall ($k_w[G]$) :

74 $\dfrac{d[G]}{dt} = -(k_{p,G}[G] + k_{w,G}[G])$

75 $k_{p,G} = \dfrac{\gamma_{eff,G} \times \omega \times S}{4} = \dfrac{1}{4}\omega \times S \times (\dfrac{1}{\gamma_{p,G}} + \dfrac{1}{\Gamma_{diff-p,G}})^{-1}$ $\qquad\qquad$ Eq.S6

$\qquad\qquad\qquad\qquad\qquad\qquad\qquad\qquad\qquad\qquad\qquad\qquad\qquad$ Eq.S7

76 $k_{w,G} = \dfrac{\gamma_{eff,G} \times \omega}{4} \times \dfrac{S_{OFR}}{V_{OFR}} = \dfrac{\omega}{D_{int}} \times (\dfrac{1}{\gamma_{w,G}} + \dfrac{1}{\Gamma_{diff-w,G}})^{-1}$

$\qquad\qquad\qquad\qquad\qquad\qquad\qquad\qquad\qquad\qquad\qquad\qquad\qquad$ Eq.S8

77 $\dfrac{1}{\Gamma_{diff-w,G}} = \dfrac{\omega \times D_{int}}{4 \times 3.66 \times D}$

$\qquad\qquad\qquad\qquad\qquad\qquad\qquad\qquad\qquad\qquad$ Eq.S9

78 Where $k_{p,G}$ and $k_{w,G}$ are the pseudo-first order loss rates to the particles' surface and to the reactor inner wall, respectively.

79 $\gamma_{eff,G}$ is an effective uptake coefficient (unitless) for gas G, such as O_3, NO, $NO_3\bullet$, NO_2, and N_2O_5. ω (m/s) is the molecular

80 speed of gas G. S_{AFR} and V_{AFR} are the inner surface area and volume of Teflon tube or the AFR. D_{int} is the inner diameter of

81 the flow reactor, such as the Teflon tube (14 mm) and AFR (105 mm). D is the gas diffusion coefficient. $\gamma_{p,G}$ and $\gamma_{w,G}$ are

82 uptake coefficients (unitless) to the particulate surface and to the AFR inner wall of gaseous G, respectively. $\Gamma_{diff,G}$ describes

83 the gas phase diffusion limited surface uptake by particles and reactor inner wall (unitless). For ultrafine particles like

84 HULIS aerosol in the current study, the heterogeneous reaction is limited by gas diffusion ($\Gamma_{diff-p,G} \gg \gamma_{p,G}$), thus Equation

85 S7 can be modified, considering also particle wall loss as:

86 $k_{p,G} = \dfrac{\gamma_{eff,G} \times \omega \times S}{4} = \dfrac{1}{4}\omega \times S \times e^{-k_{w,p}t} \times \gamma_{p,G}$

$\qquad\qquad\qquad\qquad\qquad\qquad\qquad\qquad\qquad\qquad\qquad\qquad\qquad$ Eq.S10

87 As discussed in *Scenario I*, the measured first-order wall loss rate ($k_{w,p-S}$, s^{-1}) for HULIS particle surface area concentration

88 under dry conditions is $(2.84 \pm 0.33) \times 10^{-4}$ s^{-1}. To simplify, a time-averaged $k_{p,G}$ was estimated over the residence time (RT)

89 of particles in the AFR:

$$k'_{p,G} = \frac{\int_0^{RT} k_{p,G}}{RT} = \frac{\omega \times S \times \gamma_{p,G}}{4 \times RT \times k_{w,p-S}}(1 - e^{-k_{w,p-S} \times RT}) = 0.963 \times \frac{1}{4}\omega \times S \times \gamma_{p,G} \qquad \text{Eq.S11}$$

91 When the loss rates of the gases to the reactor wall are not determined by surface reactivity, but by the diffusion through

92 the gas phase ($\gamma_{w,G} > \Gamma_{diff\text{-}w,G} \sim 7 \times 10^{-6}$), the following expression holds:

$$k_{w,G} = \frac{\omega}{D_{int}} \times (\frac{1}{\gamma_{w,G}} + \frac{1}{\Gamma_{diff-w,G}})^{-1} \approx \frac{\omega \times \Gamma_{diff-w,G}}{D_{int}} = \frac{4 \times 3.66 \times D}{D_{int}^2} \qquad \text{Eq.S12}$$

94 Equation S12 is valid for Peclet numbers in excess of ~20 [9]. The wall loss rates of NO and NO$_2$ in the Teflon tube and in

95 the AFR have been characterized using NO$_x$ analyzer (Model 49i, Thermo) with standard cylinder gases. The ozone wall

96 loss rate in the Teflon tube was measured to be around 6.67×10^{-5} s^{-1}, and the loss rate in the AFR was cited from Scenario

97 *I* experiments as average of high and medium O$_3$ conditions. The wall loss rates of O$_3$, NO, and NO$_2$ are summarized in

98 **Table S1**.

99 To NO$_3\bullet$ and N$_2$O$_5$, their wall loss rates in the current experiments were tentatively estimated based on Equation S8.

100 Diffusion coefficients were taken as 92 ± 46 and 65 ± 33 Torr cm^2 s^{-1} for NO$_3\bullet$ and N$_2$O$_5$, respectively, in air/N$_2$ environment

101 (1 atm and 296.6 K).[10] This study results in Peclet numbers above 20 for all gases in both Teflon tube and the AFR, verifying

102 the validity of Equation S12 in gaseous wall loss estimation in this work. The effective uptake coefficient (γ) depends on

103 the type of surface, the gaseous reactant, and many environmental parameters.[1,2] Overall, based on equations EqS8-S9 we

104 collected all the uptake coefficients and applied the average values of $(9.87 \pm 7.53) \times 10^{-6}$, $(1.1 \pm 0.2) \times 10^{-2}$, $(6.10 \pm 1.82) \times 10^{-5}$,

105 and $(6.73 \pm 2.36) \times 10^{-7}$ for O$_3$, NO$_3\bullet$, N$_2$O$_5$, and NO$_2$ onto biomass burning related organic aerosols, respectively.[11,12]

106 Accordingly, the first-order loss rate of gaseous species to HULIS particles were calculated and are presented in **Table S1**.

107

108 **Table S1**. Parameters estimated for Chemical box model simulation.

Scenario I and II (Pristine O$_3$ oxidation)	k_{w,O_3} in AFR (s^{-1})	$k_{w,p\text{-}S}$ in AFR (s^{-1})	$k_{w,p\text{-}V}$ in AFR (s^{-1})	γ_{eff,O_3}
Dry, 5 ppm O$_3$	$(2.62 \pm 0.22) \times 10^{-5}$	$(2.84 \pm 0.33) \times 10^{-4}$	$(2.30 \pm 0.36) \times 10^{-4}$	$(8.10 \pm 1.57) \times 10^{-5}$
Dry, 15 ppm O$_3$	$(2.26 \pm 0.17) \times 10^{-5}$	$(2.84 \pm 0.33) \times 10^{-4}$	$(2.30 \pm 0.36) \times 10^{-4}$	$(6.28 \pm 1.15) \times 10^{-5}$
Dry, 25 ppm O$_3$	$(1.96 \pm 0.20) \times 10^{-5}$	$(2.84 \pm 0.33) \times 10^{-4}$	$(2.30 \pm 0.36) \times 10^{-4}$	$(5.91 \pm 1.07) \times 10^{-5}$
30% RH, 25 ppm O$_3$	$(3.63 \pm 0.51) \times 10^{-5}$	$(5.22 \pm 0.49) \times 10^{-4}$	$(4.25 \pm 0.39) \times 10^{-4}$	$(1.02 \pm 0.13) \times 10^{-4}$
45% RH, 25 ppm O$_3$	$(4.09 \pm 0.52) \times 10^{-5}$	$(6.54 \pm 0.40) \times 10^{-4}$	$(5.58 \pm 0.30) \times 10^{-4}$	$(1.13 \pm 0.14) \times 10^{-4}$
75% RH, 25 ppm O$_3$	$(8.83 \pm 0.75) \times 10^{-5}$	$(9.80 \pm 0.53) \times 10^{-4}$	$(7.49 \pm 0.44) \times 10^{-4}$	$(1.84 \pm 0.24) \times 10^{-4}$

| Scenario III | Peclet Number | | first-order loss rate (s^{-1}) | | |
	Teflon tube (low NO$_x$, 1ppm NO)	AFR	$k_{w,G}$ in Teflon tube	$k_{w,G}$ in AFR	$k'_{p,G}$ in AFR
NO	58 ± 20	51 ± 18	< 0.0001	< 0.0001	---
O$_3$	68 ± 4	60 ± 4	$(6.67 \pm 0.67) \times 10^{-5}$	$(2.11 \pm 0.19) \times 10^{-5}$	$(1.59 \pm 0.30) \times 10^{-4}$
NO$_2$	65 ± 23	58 ± 20	$(1.04 \pm 0.36) \times 10^{-4}$	$(5.16 \pm 1.80) \times 10^{-4}$	$(1.79 \pm 0.63) \times 10^{-6}$

NO$_3$•	75 ± 38	67 ± 33	0.90 ± 0.45	(1.61 ± 0.80)×10^{-2}	(2.50 ± 0.46)×10^{-2}
N$_2$O$_5$	106 ± 54	95 ± 48	0.64 ± 0.32	(1.14 ± 0.56)×10^{-2}	(1.16 ± 0.32)×10^{-4}
Particles	---	---	---	(2.84 ± 0.33)×10^{-4}	---

109 Note: $k_{w,O3}$ is the first-order wall loss rate of O$_3$, $k_{w,p-S}$ and $k_{w,p-V}$ indicate first-order wall loss rate of bulk aerosol surface area and

110 volume concentration, respectively. $\gamma_{eff,O3}$ indicates the effective surface uptake coefficient of O$_3$ by HULIS particles. $k_{w,G}$ and $k'_{p,G}$

111 denote pseudo-first order loss rate of corresponded gaseous species to inner wall and particles, respectively.

112 Applying the above simplified kinetic parameters, a chemical box model including gaseous NO$_3$• formation and gaseous

113 oxidants uptake by HULIS aerosol and by the reactor wall was initialized using the COPASI software (complex pathway

114 simulator, http://copasi.org/), and the result for low and high NO$_x$ experiments are displayed in Figure S3. By comparing

115 the measured O$_3$ concentration changes with box-model simulated ones, the box-model worked well although it gave

116 slightly higher O$_3$ concentrations.
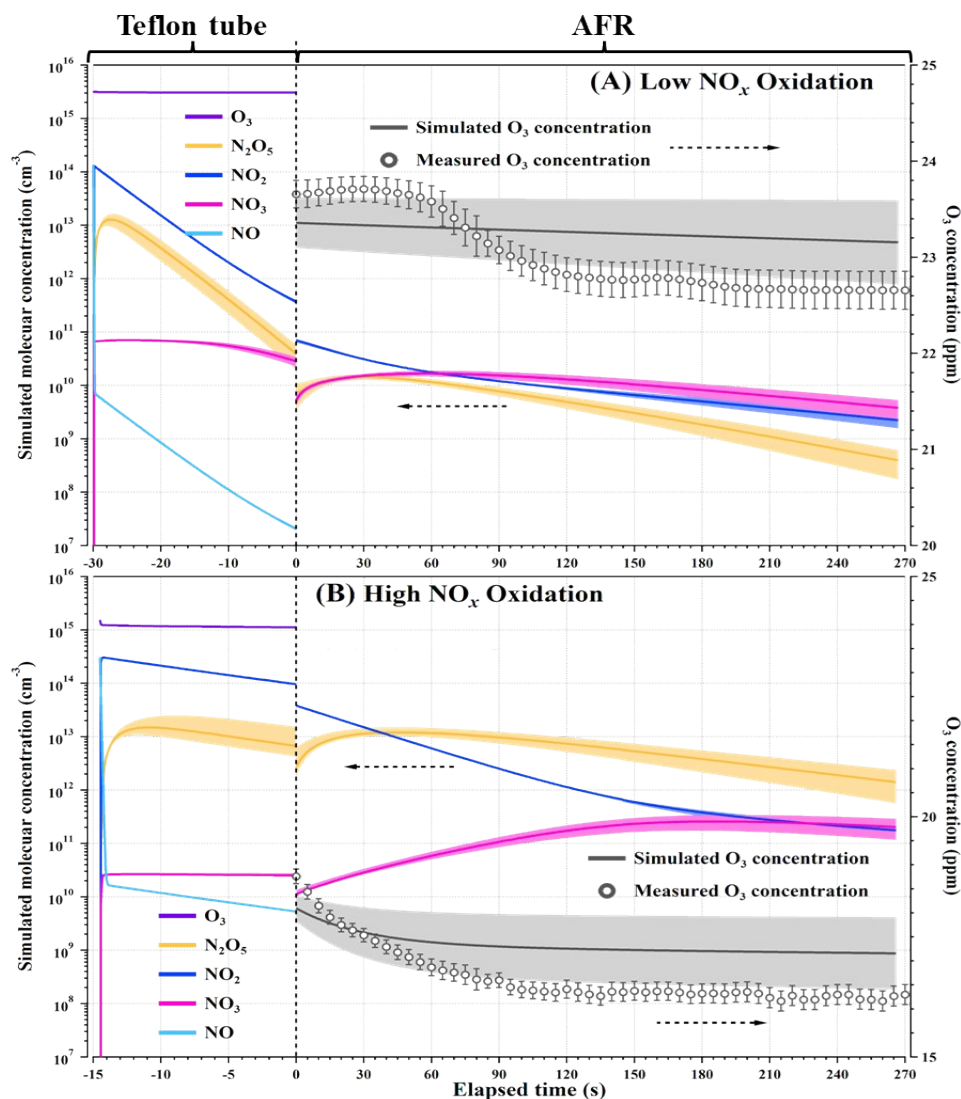
Fig. S3. Box-model simulated gaseous oxidants evolution in the Teflon tube and the AFR for NO_x-involved HULIS heterogeneous aging. The monitored O_3 concentration changes were compared with the box-model simulated results.

$NO_3•$ exposure ($[NO_3]_{exp}$, molecules cm^{-3} s) was estimated for HULIS particles in the AFR:

$$[NO_3•]_{exp} = \int_0^{HR} [NO_3]dt$$

Eq.S13

For low NO_x-O_3 oxidation, $NO_3•$ exposure was $(5.78\pm1.07)\times10^{12}$ molecules cm^{-3} s. The corresponding exposure upon high NO_x level oxidation was $(4.26\pm0.84)\times10^{13}$ molecules cm^{-3} s. Assuming a typical concentration of 20 ppt for field $NO_3•$ at night, the estimated $NO_3•$ exposures in the AFR equals to 3.3 ± 0.6 and 24.2 ± 4.8 hours' exposure of ambient nighttime $NO_3•$, respectively.

In addition, the modeled $NO_3•$ uptake by HULIS particles was $(2.43\pm0.68)\times10^{11}$ and $(8.91\pm2.21)\times10^{11}$ molecules cm^{-3} at low and high NO_x condition, respectively. The equivalent field exposure time (t) can also be calculated via Equation S14:

$$t = \frac{F}{k'_{P,NO3} \times [NO_3•]}$$

Eq.S14

8

128   Where F is NO$_3$• uptake by HULIS particles, $k_{p,G}^{'}$ is first-order NO$_3$• loss rate to HULIS particles (summarized in Table

129   S1), $[NO_3\cdot]$ is field average NO$_3$• concentration (20 ppt). Accordingly, the final equivalent filed exposure time was 5.5±1.9

130   and 20.2±6.2 hours, which are quite similar to the values estimated via NO$_3$• exposure method.

Text S2. UHPLC-PDA-ESI(-/+)-HRMS analysis

Four HULIS samples (fresh, 25ppm O_3 oxidized under dry and 45% RH, and highly $NO_3\bullet$ oxidized) were extracted into acetonitrile (Optima LC/MS grade, Fisher Chemical) via sonication (Quantrex 140 sonicator). The final solutions were filtrated using PTFE syringe filters (0.2 μm pore size, Thermo Scientific) and adjusted to about 100 μg mL^{-1} HULIS in acetonitrile. An operational blank was prepared by performing the same extraction procedure.

Samples were injected into a Luna Omega Polar C18 UHPLC reversed-phase column (2.1 mm × 50 mm, 1.6 μm particles, 100 Å pores, Phenomenex Inc.). The injection volume of each sample was 30 μL to achieve 3 μg injected mass of HULIS, assuming that injected mass was equivalent to organic material mass.

Gradient elution was performed by adapting the HPLC method from Lin et al (2018) [13] to a corresponding UHPLC method with a constant flow rate of 0.4 mL/min: 10% acetonitrile at 0-0.5 min, linear gradient to 100% acetonitrile at 0.5-16.5 min, 100% acetonitrile at 16.5-18.5 min, linear gradient back to the initial conditions at 18.5-19 min, and initial conditions at 19-24 min to recondition the column for the next sample run. Following the UHPLC separation, the eluents passed through PDA and an Orbitrap HRMS mass analyzer equipped with an ESI source. The ESI source was operated with the following conditions: spray voltage of 3 kV, capillary temperature of 300 °C, 50 units of sheath gas flow, 12 units of auxiliary gas flow, 2.5 units of spare gas flow, a maximum spray current of 100 V, a probe heater temperature of 250 °C, and an S-lens RF level of 40 V. The ESI analysis was conducted in alternating polarities.

UHPLC-PDA-ESI(−/+)-HRMS data were acquired using Thermo Scientific Xcalibur software and processed by MZmine code (http://*mzmine.github.io/*), which performed deconvolution, smoothing, and alignment of LC-MS peaks. Formulas were assigned for species within that specific time range using a suite of Excel macros and the MIDAS formula calculator (https://*nationalmaglab.org/user-facilities/icr/icr-software*).[14] The formula assignments were limited to compounds containing $C_{0\sim50}H_{0\sim100}O_{0\sim50}N_{0\sim3}$. In addition, O was indispensable in all formulas that were detected via −ESI mode. A single Na atom was allowed for assignments of MS features detected in +ESI mode. Neutral formulas for [M-H]$^-$ ionized compounds were determined by adding the mass of hydrogen. During the assignment procedure, one dimensional Kendrick Mass Defect analysis did not suggest the presence of sodium formate [M+(NaHCO$_2$)$_x$-H]$^-$ adducts in -ESI mode, therefore, they were not assigned in the HULIS samples.[15] Neutral formulas for [M+H]$^+$ and [M+Na]$^+$ ionized compounds were determined by subtracting the mass of hydrogen or sodium, respectively.

The O/C and H/C values for the Van Krevelen diagram (VK), double-bond equivalent (DBE), aromaticity index (AI), and maximum carbonyl ratio (MCR) values for molecular corridor plots were determined using the corresponding formulas of neutral CHO species.[16]

Double-bond equivalent (DBE) is calculated via Equation S15:

$$DBE = C - 0.5H + 0.5N + 1 \qquad\qquad\qquad \text{Eq.S15}$$

Aromaticity index (AI) of the assigned CHO molecule is calculated using equation S16:

$$AI = \frac{1 + C - O - 0.5H}{C - O} \qquad\qquad\qquad \text{Eq.S16}$$

164 Maximum carbonyl ratio (MCR) for only $C_C H_H O_O$ species is calculated according to Equation S17:

165 $$MCR = \frac{DBE}{O}$$ 　　　　　　　　　　　　　　　　　　　Eq.S17

166 The C, H , and O indicates element numbers in assigned CHO formulas. Noteworthy, MCR indicates the maximum criteria

167 for the presence of carbonyl functionalities. If the number of oxygen atoms in the molecule is smaller than its DBE, then

168 the MCR is considered to equal 1 (i.e., all oxygen atoms contribute to the DBE). MCR values <0.2 usually correspond to

169 very highly oxidized species, MCR values >0.2-0.5 are frequently observed in highly oxidized species, MCR values >0.5-

170 0.9 belong to intermediately oxidized species, and MCR values >0.9 suggest oxidized unsaturated and highly unsaturated

171 species.[16]

Text S3. Total peroxide (H$_2$O$_2$eq) quantification and Oxidative Potential (OP) assessment

The total peroxides, including inorganic hydrogen peroxide (H$_2$O$_2$) and organoperoxides (ROOR, ROOH) in HULIS solutions, were quantified based on the iodometric-spectrophotometric method,[17,18] in which peroxides oxidize I$^-$ in acidic conditions to generate I$_2$, and I$_2$ reacts with I$^-$ to form the yellow stable product of I$_3^-$. These color-changing reactions generally end within 1 h. Before the experiment, 1.5 g L^{-1} oxalic acid and 1.0 M KI stock solution were prepared separately in MiliQ water and bubbled with pure N$_2$ to remove dissolved oxygen overnight. H$_2$O$_2$ was applied as the standard chemical to create the calibration curve between the initial peroxide concentration and final solution absorbance at 350 nm and 400 nm. The method was verified by incubating a mixture of 2.2 mL oxalic acid solution, 0.3 mL KI solution, and 0.5 mL deionized water or PBS *vs.* 45 and 450 µM H$_2$O$_2$ under dark and in oxygen-free conditions. Absorption by the mixture solutions was measured every 15 min from incubation. As shown in Figure S4A-B, the chromogenic reactions finished in about 1h, after which the solution absorbance stabilized for at least 1 h. Absorption calibration curves with H$_2$O$_2$ concentration in the range of 5-200 µM were generated at 350 and 400 nm (Figure S2C). There is no difference in absorbance-H$_2$O$_2$ concentration in water and PBS, only the average results were used for generating the calibration curves.
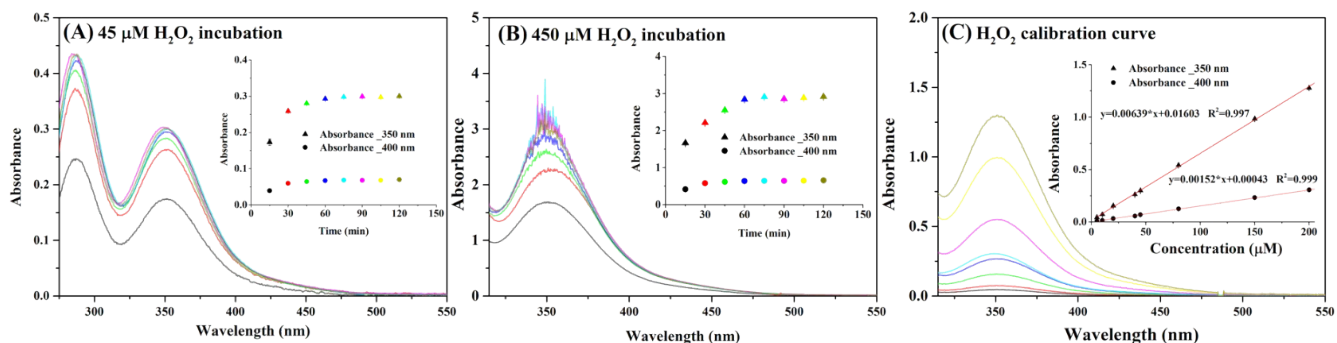

Fig. S4. Iodometric-spectrophotometric method for quantifying peroxide concentration. (A)-(B) method validation and incubation time optimization. (C) Calibration curve for standard H$_2$O$_2$ concentration and final solution absorbance after 1 h incubation.

Oxidative potential (OP) of particulate matter was measured using a modified method modified from Chao et al. (2008). Briefly, the HULIS solution was incubated with 0.1 mM DTT in PBS (0.1 M, pH7.4, Chelex 100 Sodium form resin treated) at 37 °C under dark conditions. Every 5 min, aliquot of incubated mixture was withdrawn and mixed subsequently with 10% w/v trichloroacetic acid (TCA, ≥99.0%, Sigma-Aldrich), 0.1 mM 5,5-dithio-bis-(2-nitrobenzoic acid) (DTNB, ≥99.0%, Sigma-Aldrich, prepared in PBS), and 0.4 M Tris-buffer (Trizma-base, ≥99.9%, Sigma). Remained DTT reacted with DTNB to form yellow products with specific absorbance at 412 nm. Based on the built calibration curve (Figure S5A), DTT concentration can be quantified.

Assuming a pseudo-first-order reaction, DTT depletion rate (OP^{DTT}, µmol L^{-1} min^{-1}) was derived. It was assured that less than 25% of DTT was consumed during incubation. Noteworthy, the initial absorbance (Abs_0) at 412nm was further corrected from the background absorption by HULIS. Corrected by operational blank, DTT depletion rates divided by organic carbon (OC) mass concentration in extracts give mass normalized oxidative potential (OP^{DTT}_{OC}, pmol min^{-1} µg^{-1} OC). HULIS OC mass concentration was determined using a total organic carbon analyzer (TOC-V$_{CPH}$, Shimadzu). OP for

12

standard 1,4-naphthaquinone (1,4-NQ) and H_2O_2 as positive controls were measured frequently to ensure the reliability of the DTT assay. As shown in Figure S5B-C, 1,4-naphthoquinone has perfect linear regression between concentration and DTT depletion rate, indicating the catalytic behavior of 1,4-NQ in redox reaction with DTT. While H_2O_2 roughly presents a linear relationship with DTT consumption rate, it is reasonable that peroxides act as noncatalytic oxidizers in redox cycling. Overall, the regressed normalized OP is 3.91 ± 0.27 nmol min^{-1} μmol^{-1} and 3.96 ± 0.37 nmol min^{-1} μmol^{-1} for 1,4-NQ and H_2O_2, respectively. These values agree with the reported results in relevant publications.[19,20]
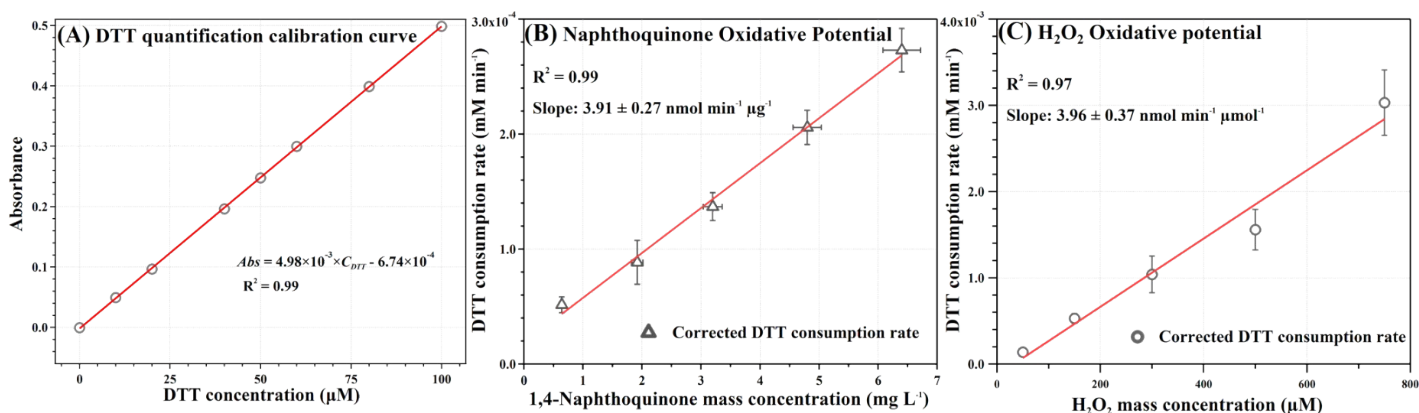
Fig. S5. (A) Calibration curve of DTT concentration vs. absorbance at 412 nm. DTT assay based oxidative potential of 1,4-Naphthoquinone (B) and hydrogen peroxides (C).

13

Text S4. Gallic equivalent phenolic assay (GAE) and Trolox equivalent antioxidant capacity (TEAC)

Folin-Ciocalteu's phenol (FC) reagent assay was applied to quantify GAE in HULIS.[21] To avoid unexpected radical scavenging, no organic solvent (e.g., methanol, ethanol, acetone, etc.) was used in the assay. Briefly, gallic acid (97.5-102.5%, Product No. G7384, Sigma-Aldrich) stock solutions in molar concentration range of 50-300 μM (50, 75, 100, 125, 150, 200, 250, 300 μM) were prepared in both deionized water and PBS. 0.45 mL stock solution of each concentration mixed with 0.05 mL FC reagent (F9252, Sigma-Aldrich) at room temperature for 6 min. Then it was mixed with 1.0 mL of 4.5 % *w:v* Na_2CO_3 (>99%, Merck) and incubated at 37 °C for 30 min. The final solution absorbance in wavelength range of 200-850 nm (0.5 nm resolution) was recorded using an Ocean-optic UV-Vis spectrometer (USB650). The linear regression between blank-corrected characteristic absorption at 750 nm and gallic acid concentration was developed as calibration curve of GEA. The result is displayed in Figure S6A-B.

ABTS free radical scavenging method was applied to provide TEAC of HULIS samples. In test, stock solution of ABTS (2,2′-azino-di-(3-ethylbenzthiazoline sulfonic acid), A3219, Sigma-Aldrich) was ready to use. 5 mM Trolox in PBS (1.0×, Biological Industries) was prepared, then diluted to 5-125 μM (5, 10, 25, 50, 75, 100, 125 μM) in MiliQ water and PBS as stock solutions. 9.8 mM potassium persulfate (≥99%, Merck) was prepared freshly, and mixed with ABTS solution in volume ratio of 1:3. The mixture was kept in the dark at room temperature for 16 h. The produced $ABTS^{\bullet+}$ in blue-green color was stable and used within 6 h. Before use, $ABTS^{\bullet+}$ solution was diluted with MiliQ water to absorption of 0.7 (±0.02) at 734 nm. Then, 1.0 mL diluted $ABTS^{\bullet+}$ solution and 0.2 mL Trolox solution was mixed at room temperature, the absorption of the mixture was recorded continuously, the absorbance at 734 nm at exactly 6 min of incubation for Trolox (Abs_{Tro}) and blank (Abs_0) was taken. The percentages $(1-Abs_{Tro}/Abs_0)\times100\%$ against Trolox concentrations were linear-regressed as calibration curve (Figure S6C-D), via which TEAC of HULIS samples following same testing procedures were derived. Apart from Trolox, reduced L-glutathione (GSH) and DTT were also used as standard to get better antioxidative information of HULIS in comparing with various antioxidants.

It was found that solvent (water *vs*. PBS) has no significant influence on absorption response in GAE and TEAC methods, gallic acid and trolox both present linear relationship between characteristic absorption and concentration. But to antioxidant like DTT and GSH, the solvent effect is clear and an exponential-function fits well for absorbance against concentration.

Extraction efficiency for the method (acetonitrile extraction-N_2 blow dry-DI water reconstitution) was assessed by spiking fix amount of standard trolox and gallic acid solutions onto blank Teflon filters, then these filters were treated with same extraction and chemical quantification procedures. An average recovery rate of 96.5±2.6% (95.7±3.2% for Trolox, 97.3±1.8% for Gallic acid, respectively) was estimated and applied to correct corresponded results. Besides, HULIS extraction efficiency was also assessed by measuring absorption of retained BrC on acetonitrile extracted Teflon filters, it was found that no more BrC resided on teflon filters after three times acetonitrile extraction as conducted in the methods, demonstrating the high extraction efficiency of HULIS in current study.
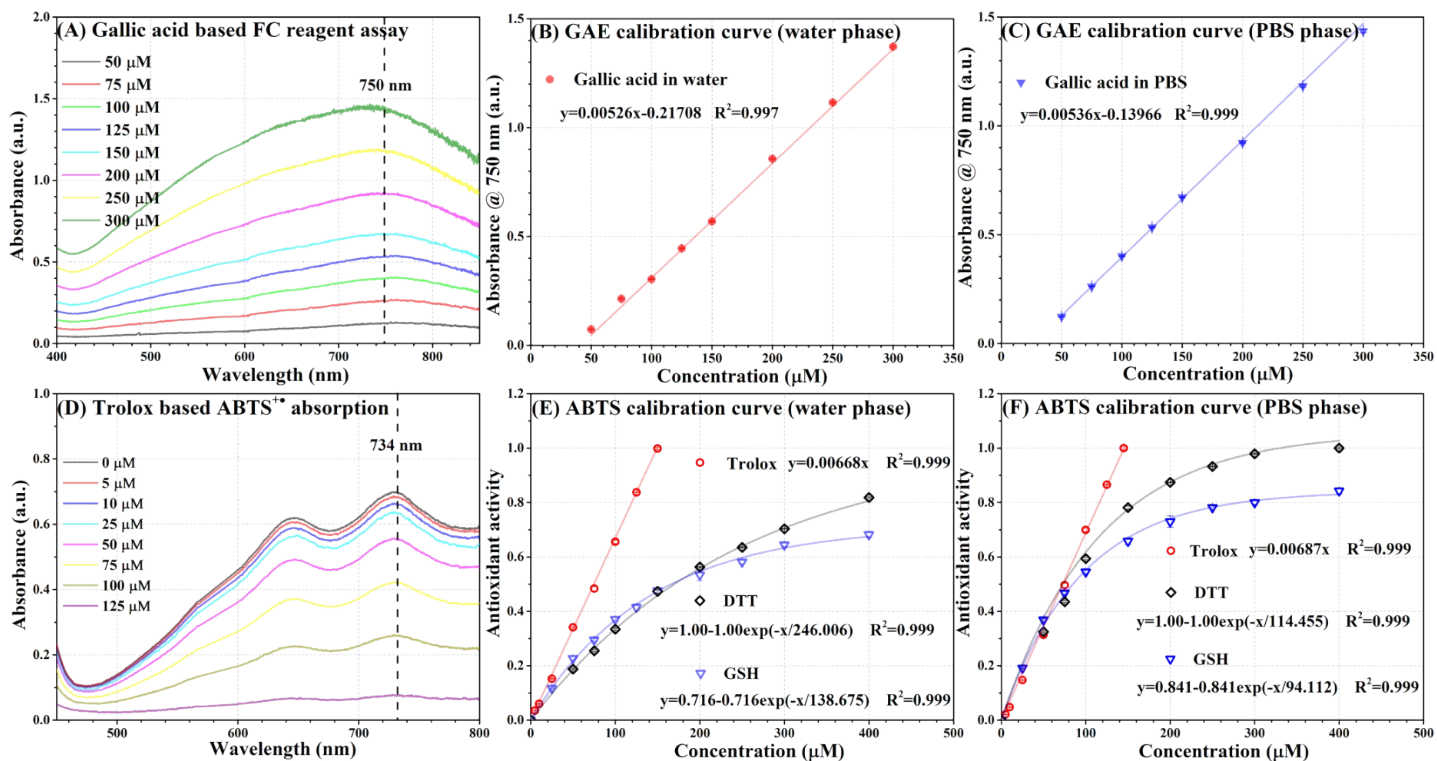
239 **Fig. S6**. Visible spectrophotometric methods in phenolic composition and antioxidant capacity determination of HULIS samples. (A)-

240 (C) calibration curve for gallic acid as reference in phenolic quantification using FC reagent assay. (D)-(R) calibration curve for trolox

241 being equivalent standard in antioxidant capacity test via ABTS radical method.

Text S5. HULIS cytotoxicity

Cell culture and exposure to HULIS extracts. The human alveolar epithelial adenocarcinoma cell line A549 (CCL-185[TM], ATCC®) were cultured in RPMI (Gibco, Thermo Fisher Scientific, MA, US) supplemented with 10% fetal bovine serum (FBS) and 5 μg mL^{-1} penicillin/streptomycin (Biological Industries) in a humidified atmosphere of 95% purified air and 5% CO_2 at 37 °C. The cells were exposed to various HULIS extracts as well as a blank control group. The HULIS extracts were used at concentrations of 200 and 300 mg OC/L in a serum-free medium containing salts and glucose. The medium comprises 50 mM HEPES, 100 mM NaCl, 5 mM KCl, 2 mM $CaCl_2$, and 5 mM glucose, with a pH of 7.2 to maintain osmolarity. The working concentrations of HULIS were determined through preliminary tests to establish appropriate range limits.

Cell viability. Cell death was assessed using propidium iodide (PI), a DNA-intercalating dye that is not taken up by viable cells. After being exposed to HULIS extracts for 5 hours, the cells were stained with 1 μg mL^{-1} of PI for 20 minutes in the dark. Subsequently, the fluorescence was measured by a flow cytometry (Amnis CellStream, Luminex, USA) with excitation (Ex) at 488 nm and emission (Em) at 610 nm. Data were collected for 10,000 cells.

ROS production. Following a 5-hour exposure to HULIS extracts, the cells were incubated with a probe solution containing 25 μM of 2′,7′-dichlorofluorescein diacetate (DCF) or dihydroethidium (DHE) for 15-20 minutes at 37 °C in the dark. The fluorescence was measured from 10,000 cells by flow cytometer (Amnis CellStream, Luminex, USA). The DCF probe fluorescence was measured at 488 nm excitation and 529 nm emission, while the DHE probe fluorescence was measured at 488 nm excitation and 620 nm emission. Within each experiment, the fluorescence intensities of cells exposed to HULIS were normalized to those of the control group. The results obtained from the DCF probe measurements were considered as the measurement of total reactive oxygen species (ROS). While, the measurements obtained from the DHE probe represented signals for the superoxide anion ($O_2\bullet-$).

Lipid peroxidation. Boron dipyrromethene difluoride (BODIPY) assay was applied to quantify lipid peroxidation from A549 cells after HULIS exposure. BODIPY solution incubated with the cells for 30 min, then levels of oxidized and unoxidized BODIPY were measured at 485/520 nm (Ex/Em) and 580/595 nm (Ex/Em), respectively. The lipid peroxidation result was represented as a ratio of oxidized to unoxidized BODIPY.

Statistical analysis. The results are expressed as the mean ± standard deviation (SD). Differences between group means were tested by one-way ANOVA with Welch modification for heteroscedastic data. Differences were considered significant at a probability level of $p < 0.05$ using Tukey's honestly significant difference hypothesis testing. The statistical analysis was performed in GraphPad #8 software and graphical displayed using OriginPro 9.0.

Table S2. Summarized HULIS chemical features and redox potentials following atmospheric heterogeneous agings

HULIS Samples	O/C	H/C	N/C	OM/OC	$OP_{OC\_PBS}^{DTT}$ (pmol min^{-1} µg^{-1} OC)	$OP_{OM\_PBS}^{DTT}$ (pmol min^{-1} µg^{-1} OM)	ABTS_*PBS* (nmol µg^{-1} OC)	GAE_*PBS* (nmol µg^{-1} OC)	Density (g cm^{-3})
Fresh	0.355±0.016	1.417±0.013	0.009±0.002	1.604±0.102	115.2±8.6	71.8±7.0	5.53±0.40	4.78±0.23	1.22
Dry 5ppm O$_3$ oxidation	0.419±0.015	1.422±0.009	0.008±0.002	1.687±0.118	114.4±7.2	67.8±6.4	4.83±0.27	4.38±0.31	1.22
Dry 15ppm O$_3$ oxidation	0.438±0.015	1.416±0.019	0.007±0.002	1.710±0.137	105.2±6.8	61.5±6.3	4.57±0.32	4.05±0.22	1.22
Dry 25ppm O$_3$ oxidation	0.454±0.012	1.411±0.017	0.009±0.002	1.733±0.108	98.4±7.9	56.8±5.8	4.38±0.29	3.85±0.24	1.20
30%RH 25ppm O$_3$ oxidation	0.535±0.036	1.395±0.009	0.010±0.003	1.843±0.157	77.9±6.8	42.3±5.2	3.78±0.25	3.44±0.20	1.23
45%RH 25ppm O$_3$ oxidation	0.629±0.028	1.386±0.011	0.006±0.001	1.961±0.094	71.9±5.4	36.7±3.9	3.28±0.27	2.89±0.17	1.25
75%RH 25ppm O$_3$ oxidation	0.721±0.034	1.381±0.012	0.009±0.002	2.087±0.132	60.9±4.0	29.2±2.7	2.54±0.13	2.00±0.12	1.25
Low-level NO$_3$• oxidation	0.442±0.013	1.405±0.013	0.022±0.004	1.772±0.090	113.4±6.4	64.1±4.9	4.83±0.31	3.86±0.24	1.22
High-level NO$_3$• oxidation	0.483±0.016	1.395±0.009	0.040±0.005	1.832±0.069	111.8±6.9	60.9±4.5	4.43±0.20	3.48±0.17	1.21

Note: elemental ratios and OM/OC were derived from AMS spectrum. Redox potential results were measured for HULIS in PBS. Dehydrated particle densities were measured using AAC-SMPS system. $OP_{OM\_PBS}^{DTT}$ and $OP_{OM\_PBS}^{DTT}$ are organic carbon (OC) and organic matter (OM) normalized OP^{DTT}, respectively.

271 **Text S6. Elemental changes in HULIS aerosol following heterogeneous aging**

272 Pseudo-first-order wall loss rates for HULIS particles through the AFR were estimated in blank tests based on SMPS

273 measurements. RH-depended ensemble particle wall losses are summarized in Table S1. In the experiments, HULIS

274 processed in the AFR were corrected for wall loss via Equation S18, then wall-loss corrected HULIS concentrations were

275 applied in the quantitative analysis of chemical changes.

$$m = \rho \times \sum_i N_i \times e^{k_{pi} t} \times \frac{\pi}{6} D_i^3$$

276 $\qquad\qquad$ Eq.S18

277 Where ρ (g cm^{-3}) is the ensemble dehydrated particle density. N_i (cm^{-3}) is the AFR output particle number concentration

278 of size bin ith. k_{pi} (s^{-1}) is the size-dependent particle wall loss rate of size bin ith. D_i is the particle diameter of size

279 bin ith. HULIS particle densities were calculated by comparing the particle aerodynamic and mobility size distributions

280 via Aerodynamic Aerosol Classifier (AAC)-SMPS system.[7] The densities for fresh and multiple processed HULIS are

281 in range of 1.20-1.25 g cm^{-3}. Particle-size resolved k_{pi} is displayed in Figure S7A.

282 $\quad$ After wall loss corrections for HULIS aerosols, the organic elemental mass concentrations were calculated based on

283 AMS results of bulk aerosol elemental features. To make it clear, HULIS aerosol mass concentrations were normalized

284 to the fresh one. The elemental mass concentration was calculated according to Equation S19:

$$e_{i,j} = \frac{m_i}{m_0} \times f_{i,j}$$

285 $\qquad\qquad$ Eq.S19

286 In Eq. S16, $e_{i,j}$ is mass concentration of element j (e.g., C, N, O, H) in ith HULIS sample (fresh and various

287 atmospherically aged HULIS). m_0 is wall loss corrected mass concentration for fresh HULIS, m_i is wall loss corrected

288 mass concentration for ith HULIS. $f_{i,j}$ is the fraction of organic elemental j in bulk aerosol i. The results for the organic

289 elemental concentration changes normalized to fresh HULIS are displayed in Figure S7B-D.
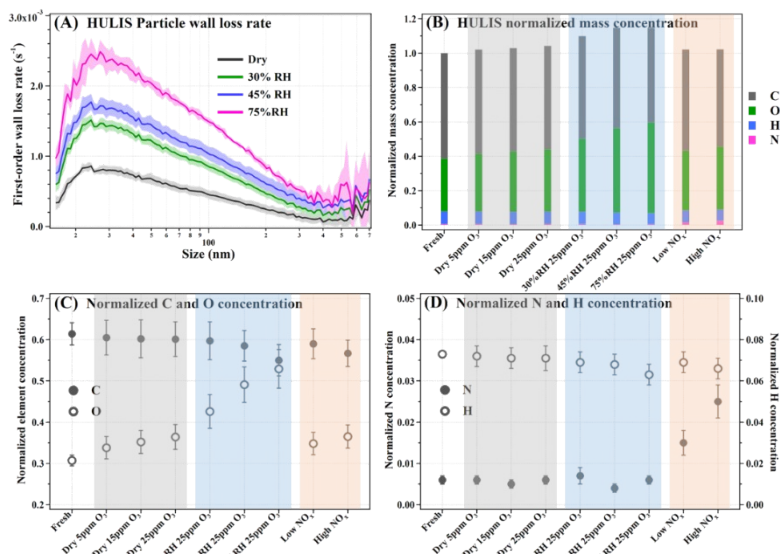

290 **Fig. S7**. (A) Size-resolved first-order wall loss rates of HULIS particles as a function of RH in the AFR; (B) The changes in

291 HULIS wall-loss corrected elemental mass concentrations that were normalized to the fresh concentrations; (C) Changes of

292 organic carbon and oxygen mass concentrations for HULIS regarding diverse aging processes; (D) Changes of organic nitrogen

293 and hydrogen mass concentrations for HULIS regarding diverse aging processes. Three shaded regions in Panel B-D indicate

294 results from dry ozonolysis (light gray), RH-influenced O_3 oxidation (light blue), and $NO_3\bullet$ oxidation (light red) of HULIS.

295
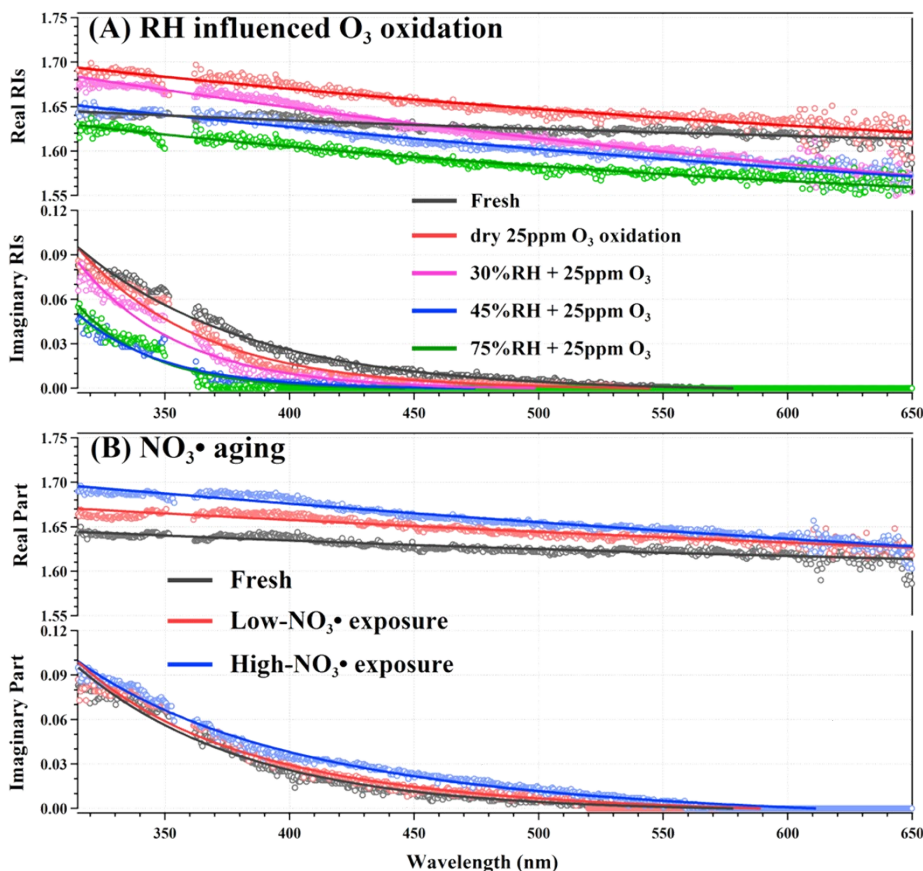
296 **Fig. S8**. The evolution of the complex Refractive Indices (RIs) of HULIS particles in heterogeneous O_3 oxidation (A) and $NO_3\bullet$ reaction

297 (B). The errors are not displayed for graphics simplification. Circles denote the raw retrieved RIs, solid lines are regression results.

298 Exponential functions were applied to regress the real part of RIs, and power-law functions were taken to depict imaginary part

299 distributions.
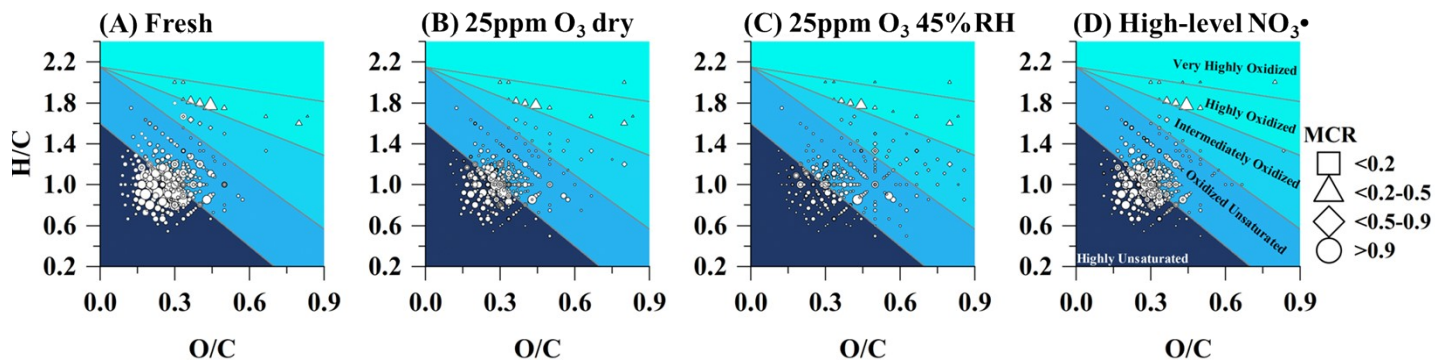
Fig. S9. MCR-VK diagrams of fresh (A) and diversely aged (B-D) HULIS. The shape of open symbol corresponds to the different MCR value range, and the size of the symbol indicates the relative intensity of formula from HRMS detection. Five compositional spaces of molecules are classified as: very highly oxidized , highly oxidized, intermediately oxidized, oxidized unsaturated, and highly unsaturated.
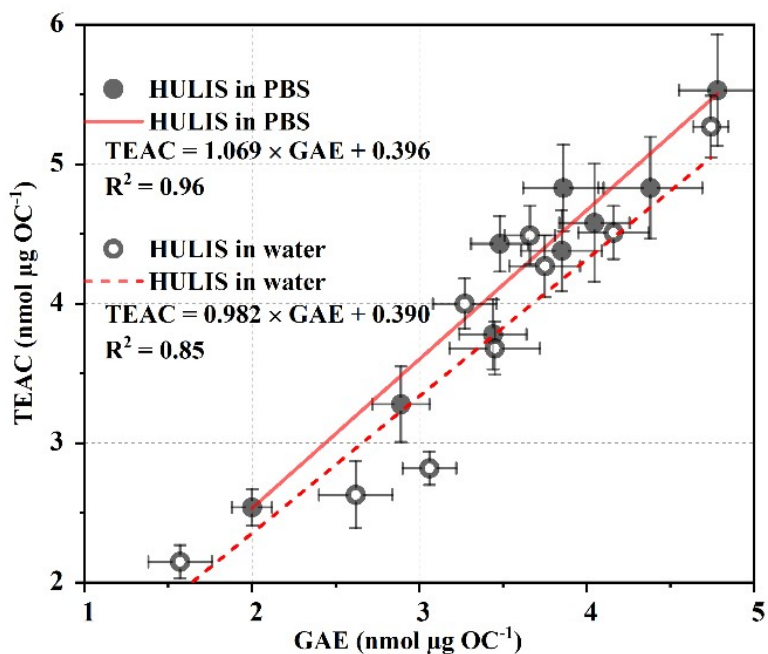
Fig. S10. Linear correlation between GAE and TEAC for HULIS in atmospheric agings.

Text S7. HULIS redox chemical lifetime during nighttime atmospheric agings

The half-lifetime ($\tau_{1/2}$) of chemicals contributing to redox potential of HULIS can be estimated from changes of wall-loss corrected HULIS concentration, mass normalized redox potential, and O_3 or $NO_3\bullet$ sink to particles in extensive agings. In short, the gaseous oxidant uptake by particles (F) after reaction time of t can be described as Equation S20 that is modified from Equation S3:

$$F_{G,P} = \kappa_{p,O3} \times [G] \times t = \frac{\gamma_{eff,G} \times \omega_G \times S_p}{4} \times [G] \times t$$

Eq. S20

Equation S20 can be further modified as:

$$F^-_{G,P} = \frac{F_{G,P}}{S_p} = \frac{\gamma_{eff,G} \times \omega_G}{4} \times [G] \times t$$

Eq. S21

Where $F^-_{G,P}$ is gaseous oxidant normalized surface uptake (molecules mm^{-2}). Thus, the half-lifetime ($\tau_{1/2}$) correlates the critical oxidant uptake that induces chemical half-decay ($F^-_{G,P_{1/2}}$):

$$F^-_{G,P/2} = \frac{\gamma_{eff,G} \times \omega_G}{4} \times [G] \times \tau_{1/2}$$

Eq. S22

$$\tau_{1/2} = \frac{4}{\gamma_{eff,G} \times \omega_G \times [G]} \times F^-_{G,P/2}$$

Eq. S23

The concentration of chemicals (C_{RP}) that contribute to antioxidant capacity and oxidative potential of HULIS was calculated via Equation S24:

$$C_{RP} = C_{OC} \times RP$$

Eq.S24

C_{OC} is wall-loss corrected particulate organic carbon mass concentration (Text S6, Figure S7), RP is short of redox potential in term of PBS solution-based GAE, TEAC, and $OP^{DTT}_{OC\_PBS}$ that are normalized to particulate organic carbon mass concentration.

We assumed that C_{RP} followed the pseudo second-order kinetic change in reaction with O_3 or $NO_3\bullet$. Therefore, the C_{RP} evolved exponentially with gaseous oxidant surface uptake or exposure, the critical gaseous oxidant surface uptake ($F^-_{G,P/2}$) that induced half-decay of C_{RP} can be derived from linear regression between $ln(\frac{C_{RP}}{C_{RP,0}})$ and $F^-_{G,P}$ for HULIS upon dry ozonolysis, RH-dependent O_3 oxidation and $NO_3\bullet$ reaction, respectively. The slopes (S_{lop}) were derived to estimate $F^-_{G,P/2}$ in Equation S25:
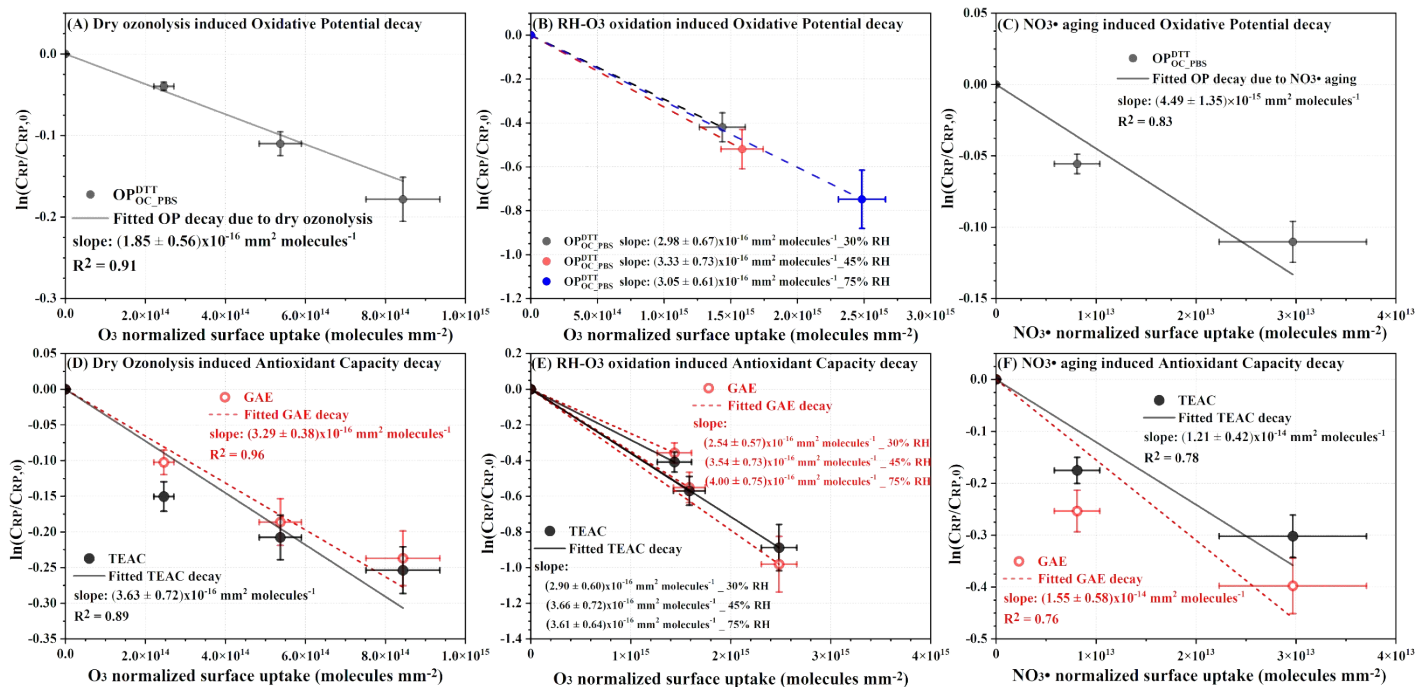
$$F^-_{G,P/2} = \frac{ln(2)}{S_{lop}}$$

Eq.S25

The linear regression and regressed slope were present in Figure S11 below. Combining Equation S23 and S25, the half-lifetime is:

$$\tau_{1/2} = \frac{4}{\gamma_{eff,G} \times \omega_G \times [G]} \times \frac{ln(2)}{S_{lop}}$$

Eq. S26

Meantime, the effective second-order reaction kinetic ($K_{RP,G}$) between RP and gaseous oxidant G can be calculated as:

$$K_{RP,G} = \frac{1}{4}\gamma_{eff,G} \times \omega_G \times S_{lop}$$

Eq. S27

Fig. S11. Linear correlation between HULIS borne redox chemical decay and gaseous oxidant normalized surface uptake. A-C profile oxidative potential contributor decay due to O_3 or $NO_3\bullet$ oxidation. D-F display antioxidant capacity contributor decay upon O_3 or $NO_3\bullet$ aging.

According to O_3 sink analysis in the AFR (Text S1), the HULIS particle effective surface uptake coefficient ($\gamma_{eff,O3}$) of O_3 was a function of O_3 concentration (ppm) or RH (%). The functions regarding dry (Eq. S28) and humidity (Eq. S30) conditions were described in Figure S2 and presented below:

$$\gamma_{eff,O3} = 5.82 \times 10^{-5} + 5.11 \times 10^{-5} \times e^{-0.16 \times [O_3]} \qquad \text{Eq. S28}$$

$$\gamma_{eff,RH} = -2.18 \times 10^{-5} + 8.04 \times 10^{-5} \times e^{\frac{RH}{77.56}} \qquad \text{Eq.S29}$$

Equation S29 is built on initial O_3 concentration of 25 ppm, to extrapolate RH effect on $\gamma_{eff,O3}$ at other O_3 level, we assumed that $\gamma_{eff,O3}$ scales with that in RH effect on the basis of dry condition, thus, integrated $\gamma_{eff,O3,RH}$ can be derived:

$$\gamma_{eff,O3,RH} = \gamma_{eff,O3} \times \frac{\gamma_{eff,RH}}{\gamma_{eff,0\% RH}} = (5.82 \times 10^{-5} + 5.11 \times 10^{-5} \times e^{-0.16 \times [O_3]}) \times (1.37 \times e^{\frac{RH}{77.56}} - 0.37) \qquad \text{Eq. S30}$$

To $NO_3\bullet$ aging, a fixed effective uptake coefficient ($\gamma_{eff,NO3\cdot}$) of $(1.1\pm0.2)\times10^{-2}$ was applied as discussed in Text S1. Above all, the half-lifetime of HULIS redox active compositions in reaction with O_3 or $NO_3\bullet$ were sensitively estimated with varying field average O_3 concentration of 5-75 ppb and $NO_3\bullet$ concentration of 5-100 ppt. The results are displayed in Figure S12. The effective second-order reaction kinetics ($K_{RP,G}$) between RP and O_3 or $NO_3\bullet$ were calculated and summarized in Table 1.
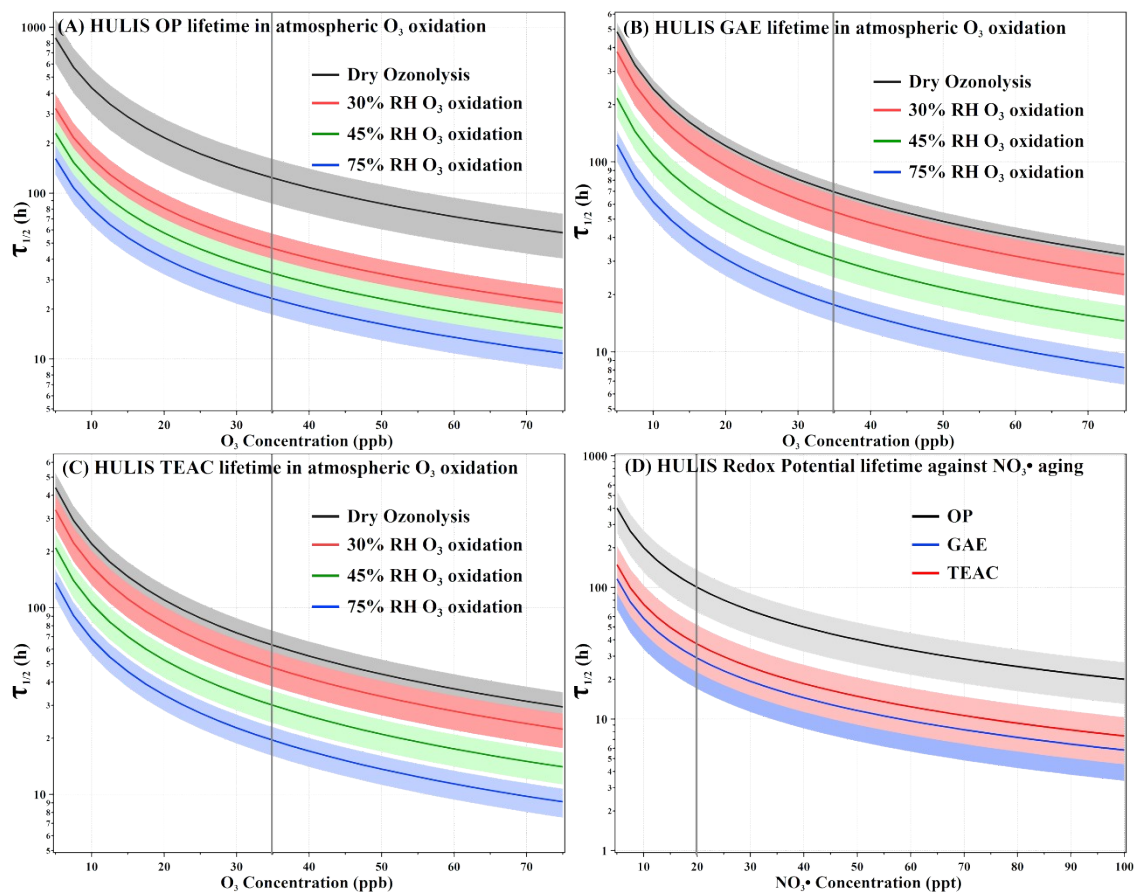
Fig. S12. Half-lifetime of HULIS redox potential against atmospheric O_3 or $NO_3\bullet$ oxidation as a function of gaseous oxidant concentration. The solid gray line indicates lifetime corresponding to the commonly applied filed average oxidant concentration, which is 35ppb for O_3 and 20ppt for $NO_3\bullet$.

23
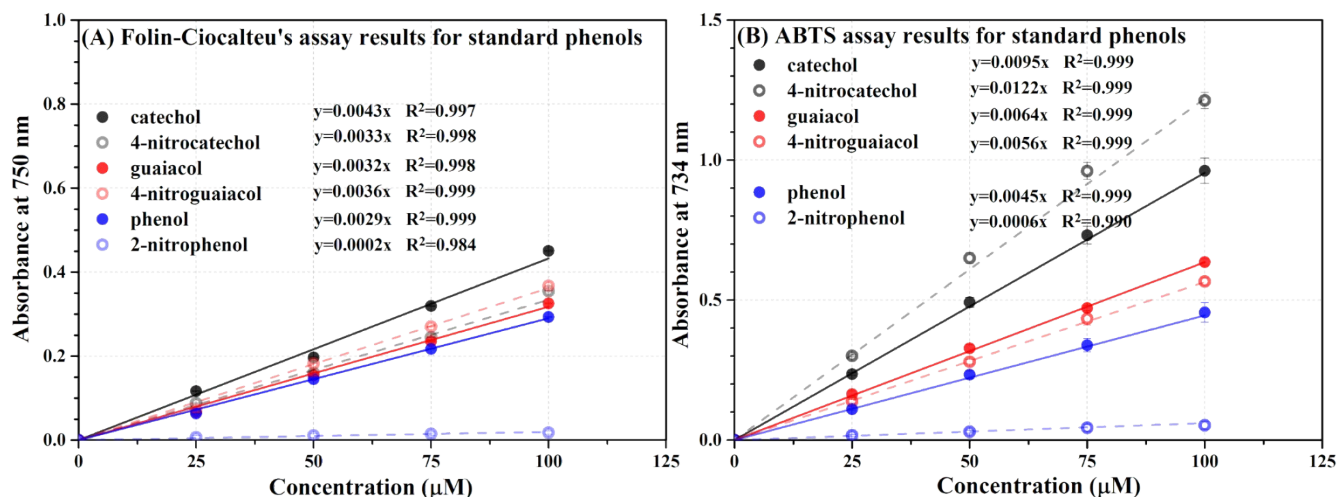
356 **Fig. S13**. Calibration function comparison between phenols and their corresponded nitrophenols in FC and ABTS assays.
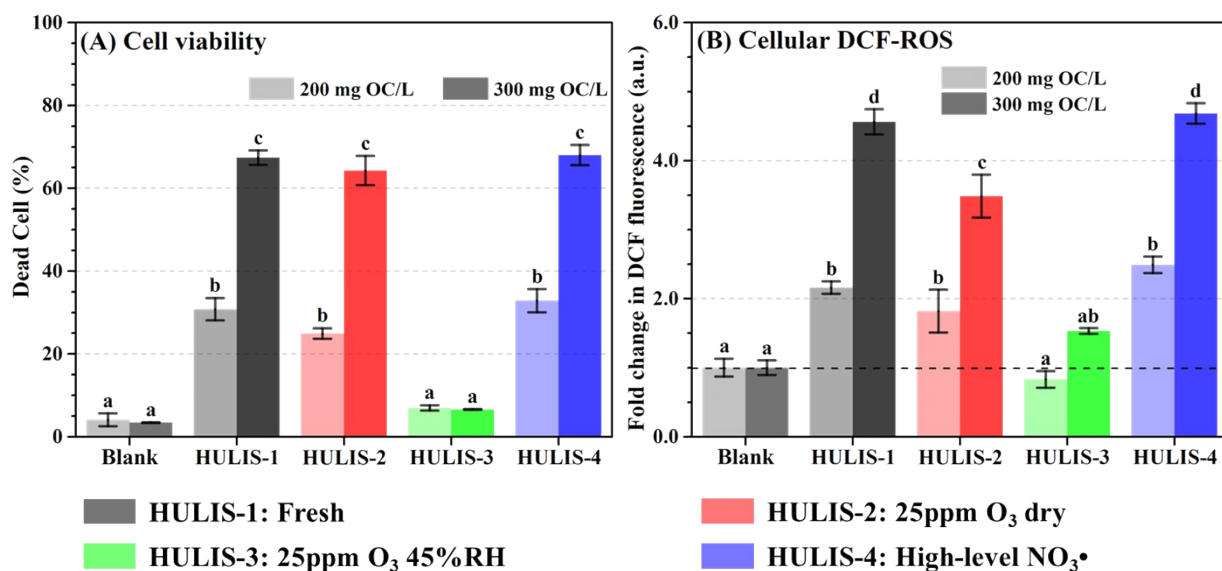

357 **Fig. S14.** Cell viability and ROS after HULIS exposure in A549. Cell viability (A) and ROS generation (B) following 5 h exposure to

358 HULIS at concentration of 200 *vs*. 300 mg OC L^{-1}. Four types of HULIS from various atmospheric process were tested. Bar height and

359 error bars represent arithmetic mean ± SEM of cell death and florescence normalized to blank values. Mean with different letters are

360 significant different at $p < 0.05$ (Turkey HSD test). Four kinds of atmospheric processed HULIS were tested, including fresh one

361 (HULIS-1), 25ppm O_3 oxidized samples under dry (HULIS-2) and at 45%RH (HULIS-3) conditions, and high-level NO_3• oxidized

362 samples   (HULIS-4).
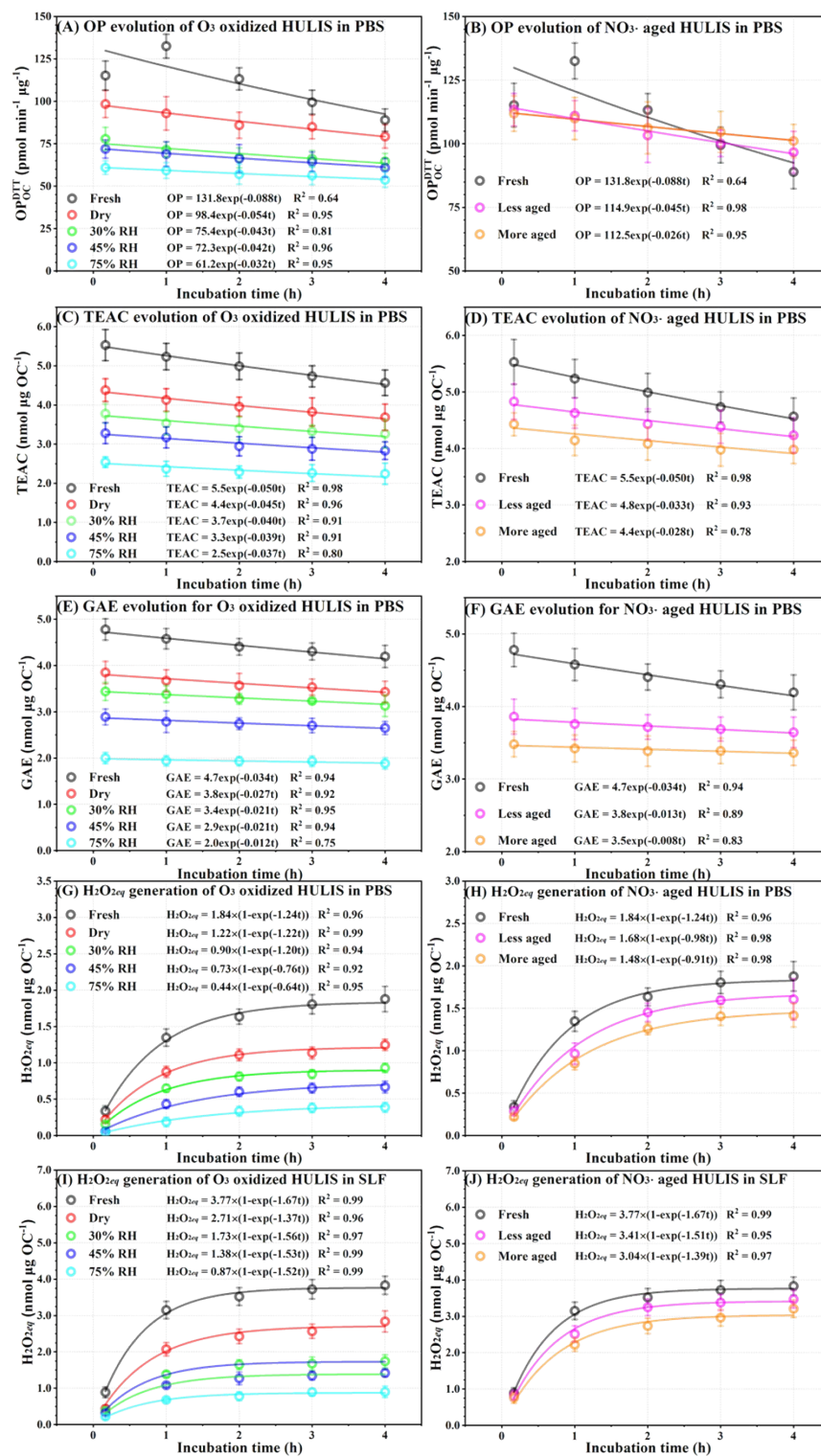
Fig. S15. Redox potential and equivalent H_2O_2 (H_2O_2eq) generation evolution for fresh and atmospheric aged HULIS in PBS and surrogated lung fluid solutions over the course of 4 h incubation openly at 37 °C in the dark. These HULIS were heterogeneously aged from RH-influenced O_3 oxidation and varying $NO_3\bullet$ reactions. The results for redox potentials and H_2O_2eq were exponentially regressed in functions of Exp2PMod1 and BoxLucas1, respectively, using OriginPro 2021.

367 **Text S8. Simplified investigation of standard redox-active compounds in lung fluid environment**

368 1,4-Naphthaquinone (1,4-NQ) and Gallic acid were selected as standard redox-active compounds to quantify the relative redox potential of HULIS in current study.

369 These components were further used as proxy to illustrate the mechanisms for HULIS aqueous aging results at neutral lung fluid environment. Following the same

370 treatment to HULIS, 5 mg L^{-1} 1,4-NQ, 25 mg L^{-1} gallic acid, and their mixture were incubated in PBS solutions (pH 7.4) at 37 °C under oxic condition for 4 hours.

371 In every one hour since incubation, the OP^{DTT}, GAE and H$_2$O$_2$eq were measured for each solution. The results are displayed in Figure S16. It was found that 1,4-NQ

372 had no signal response to Folin-Ciocalteu's assay or ABTS assay during the entire incubation period. The constant OP^{DTT} and negligible H$_2$O$_2$eq generation indicated

373 stability of sole 1,4-NQ in PBS. There was no OP^{DTT} or H$_2$O$_2$eq measured for gallic acid solution, and 4 hours' incubation did not pose significant change to the

374 mass concentration of gallic acid. Interestingly, the mixture of 1,4-NQ and gallic acid replicated the observed evolution pattern of HULIS that both the OP^{DTT} and

375 GAE decreased in coupling with H$_2$O$_2$eq generation along with incubation. Noteworthy, the rates of redox potential changes and H$_2$O$_2$eq generation were different
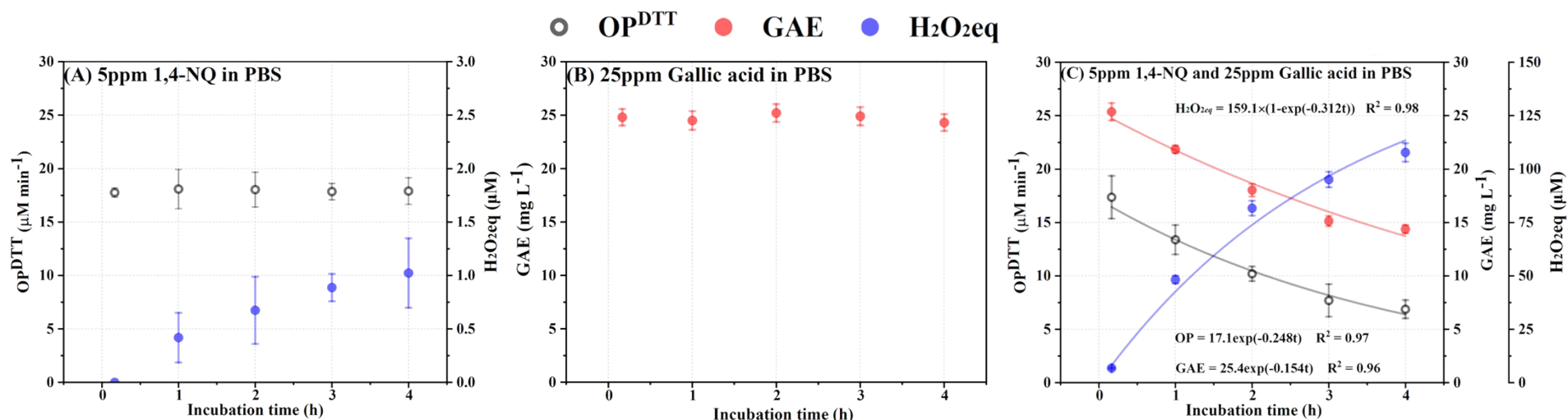
376 with that of HULIS, probably because of the more complicated redox-active compositions in HULIS.

377 **Fig. S16**. Simplified tests of 1,4-naphthaquinone (1,4-NQ for short), gallic acid, and their mixture in PBS solution over 4 hours' incubation at oxic condition and 37

378 °C. (A) Time-resolved OP^{DTT} and H$_2$O$_2$eq generation for 1,4-naphthaquinone of 5 mg L^{-1}. (B) Mass concentration changes for 25 mg L^{-1} gallic acid. (C) Evolution of

379 OP^{DTT}, H$_2$O$_2$eq, and gallic acid mass concentration for a mixture of 5 mg L^{-1} 1,4-naphthaquinone and 25 mg L^{-1} gallic acid.

26

Reference.

1 J. N. Crowley, M. Ammann, R. A. Cox, R. G. Hynes, M. E. Jenkin, A. Mellouki, M. J. Rossi, J. Troe and T. J. Wallington, Evaluated kinetic and photochemical data for atmospheric chemistry: Volume V–heterogeneous reactions on solid substrates, *Atmospheric Chemistry and Physics*, 2010, **10**, 9059–9223.

2 P. Davidovits, C. E. Kolb, L. R. Williams, J. T. Jayne and D. R. Worsnop, Mass accommodation and chemical reactions at gas− liquid interfaces, *Chemical reviews*, 2006, **106**, 1323–1354.

3 M. Li, H. Su, G. Li, N. Ma, U. Pöschl and Y. Cheng, Relative importance of gas uptake on aerosol and ground surfaces characterized by equivalent uptake coefficients, *Atmospheric Chemistry and Physics*, 2019, **19**, 10981–11011.

4 Y. Rudich, N. M. Donahue and T. F. Mentel, Aging of organic aerosol: Bridging the gap between laboratory and field studies, *Annu. Rev. Phys. Chem.*, 2007, **58**, 321–352.

5 C. Baduel, M. E. Monge, D. Voisin, J.-L. Jaffrezo, C. George, I. E. Haddad, N. Marchand and B. D'Anna, Oxidation of atmospheric humic like substances by ozone: a kinetic and structural analysis approach, *Environmental science & technology*, 2011, **45**, 5238–5244.

6 T. Berkemeier, S. S. Steimer, U. K. Krieger, T. Peter, U. Pöschl, M. Ammann and M. Shiraiwa, Ozone uptake on glassy, semi-solid and liquid organic matter and the role of reactive oxygen intermediates in atmospheric aerosol chemistry, *Physical Chemistry Chemical Physics*, 2016, **18**, 12662–12674.

7 C. Li, Q. He, Z. Fang, S. S. Brown, A. Laskin, S. R. Cohen and Y. Rudich, Laboratory Insights into the Diel Cycle of Optical and Chemical Transformations of Biomass Burning Brown Carbon Aerosols, *Environmental science & technology*, 2020, **54**, 11827–11837.

8 C. Li, Q. He, A. P. S. Hettiyadura, U. Käfer, G. Shmul, D. Meidan, R. Zimmermann, S. S. Brown, C. George and A. Laskin, Formation of secondary brown carbon in biomass burning aerosol proxies through NO_3 radical reactions, *Environmental science & technology*, 2019, **54**, 1395–1405.

9 A. Zasypkin, V. M. Grigor'eva, V. N. Korchak and Y. M. Gershenson, A formula for summing of kinetic resistances for mobile and stationary media: I. Cylindrical reactor, *Kinetics and catalysis*, 1997, **38**, 772–781.

10 M. J. Tang, R. A. Cox and M. Kalberer, Compilation and evaluation of gas phase diffusion coefficients of reactive trace gases in the atmosphere: volume 1. Inorganic compounds, *Atmospheric Chemistry and Physics*, 2014, **14**, 9233–9247.

11 S. Gross, R. Iannone, S. Xiao and A. K. Bertram, Reactive uptake studies of NO_3 and N_2O_5 on alkenoic acid, alkanoate, and polyalcohol substrates to probe nighttime aerosol chemistry, *Physical Chemistry Chemical Physics*, 2009, **11**, 7792–7803.

12 S. Gross and A. K. Bertram, Reactive uptake of NO_3, N_2O_5, NO_2, HNO_3, and O_3 on three types of polycyclic aromatic hydrocarbon surfaces, *The Journal of Physical Chemistry A*, 2008, **112**, 3104–3113.

13 P. Lin, L. T. Fleming, S. A. Nizkorodov, J. Laskin and A. Laskin, Comprehensive molecular characterization of atmospheric brown carbon by high resolution mass spectrometry with electrospray and atmospheric pressure photoionization, *Analytical chemistry*, 2018, **90**, 12493–12502.

14 P. J. Roach, J. Laskin and A. Laskin, Higher-order mass defect analysis for mass spectra of complex organic mixtures, *Analytical chemistry*, 2011, **83**, 4924–4929.

15 E. Kendrick, A mass scale based on CH2 = 14.0000 for high resolution mass spectrometry of organic compounds., *Analytical Chemistry*, 1963, **35**, 2146–2154.

16 Y. Zhang, K. Wang, H. Tong, R.-J. Huang and T. Hoffmann, The maximum carbonyl ratio (MCR) as a new index for the structural classification of secondary organic aerosol components, *Rapid Communications in Mass Spectrometry*, 2021, **35**, e9113.

17 S. Wang, J. Ye, R. Soong, B. Wu, L. Yu, A. J. Simpson and A. W. Chan, Relationship between chemical composition and oxidative potential of secondary organic aerosol from polycyclic aromatic hydrocarbons, *Atmospheric Chemistry and Physics*, 2018, **18**, 3987–4003.

18 S. Wang, M. Takhar, Y. Zhao and A. W. H. Chan, Dynamic Oxidative Potential of Organic Aerosol from Heated Cooking Oil, *ACS Earth and Space Chemistry*, 2021, 1150–1162.

19 Jiang, Ahmed, Canchola, Chen, and Lin, Use of Dithiothreitol Assay to Evaluate the Oxidative Potential of Atmospheric Aerosols, *Atmosphere*, 2019, **10**, 571.

20 C. Li, Z. Fang, H. Czech, E. Schneider, C. P. Rüger, M. Pardo, R. Zimmermann, J. Chen, A. Laskin and Y. Rudich, pH modifies the oxidative potential and peroxide content of biomass burning HULIS under dark aging, *Science of The Total Environment*, 2022, 155365.

21 S. Kupina, C. Fields, M. C. Roman and S. L. Brunelle, Determination of total phenolic content using the Folin-Ciocalteu assay: Single-laboratory validation, First action 2017.13, *Journal of AOAC International*, 2018, **101**, 1466–1472.